Available online at www.sciencedirect.com
ScienceDirect
Journal of Sound and Vibration 300 (2007) 50–70
JOURNAL OF SOUND AND VIBRATION
www.elsevier.com/locate/jsvi

Axial flow fan broad-band noise and prediction

Thomas Carolus*, Marc Schneider, Hauke Reese

Department of Fluid and Thermodynamics, University of Siegen, 57068 Siegen, Germany

Received 7 November 2005; accepted 19 July 2006
Available online 10 October 2006

Abstract

Two prediction methods for broad-band noise of low-pressure axial fans are investigated. Emphasis is put on the interaction noise due to ingested turbulence. The numerical large eddy simulation (LES) is applied to predict the unsteady blade forces due to grid generated highly turbulent inflow; the blade forces are then fed into an analytical two-dimensional acoustic ducted source model. A simple semi-empirical noise prediction model (SEM) is utilized for indicative comparison. Finally, to obtain a database for detailed verification, the turbulence statistics for a variety of different inflow configurations are determined experimentally using hot wire anemometry and a correlation analysis. In the limits of the necessary assumptions the SEM predicts the noise spectra and the overall sound power surprisingly well without any further tuning of parameters; the influence of the fan operating point and the nature of the inflow is obtained. Naturally, the predicted spectra appear unrealistically "smooth", since the empirical input data are averaged and modeled in the frequency domain. By way of contrast the LES yields the fluctuating forces on the blades in the time domain. Details of the source characteristics and their origin are obtained rather clearly. The predicted effects of the ingested turbulence on the fluctuating blade forces and the fan noise compare favorably with experiments. However, the choice of the numerical grid size determines the maximal resolvable frequency and the computational cost. As contrasted with the SEM, the cost for the LES-based method are immense.

1. Problem statement

The aeroacoustic noise of low Mach number axial fans either results from the encounter of blades with space and/or time-varying disturbances (interaction noise) or the flow over the blades themselves (self-noise). Axial-flow fans, used e.g. in air conditioning systems, are often subjected to poor inflow conditions which range from steady state but spatially asymmetric velocity profiles—due to imperfect intake geometry—to time-varying ingested vortices, turbulence or secondary inflow distortions. The resulting periodic and/or random forces cause tonal and/or broad-band interaction noise. On the other hand, if the inflow is homogeneous in time and space, the force fluctuations due to the turbulent boundary layer (TBL) on the blade surfaces and their interaction with the trailing edge (TE) and the vortex shedding from the blunt TE cause the unavoidable self-noise of the fan which in most cases is broad-band. This study is intended to contribute to the prediction of broad-band fan noise with an emphasis on the interaction noise due to ingested turbulence.

*Corresponding author. Tel.: +49 271 740 2386; fax: +49 271 740 2388.
E-mail address: carolus@ift.mb.uni-siegen.de (T. Carolus).

0022-460X/$ - see front matter © 2006 Elsevier Ltd. All rights reserved.
doi:10.1016/j.jsv.2006.07.025

Nomenclature

a	bar width of square-mesh array
A_C	correlation area
c_0	speed of sound
c	flow velocity in the stationary frame of reference
$c_{x,m}$	averaged axial flow through duct without obstructions, $(\dot{V}/(\pi r_a^2 - \pi r_i^2))$
C	chord length
D	impeller diameter, inner diameter of duct $(=2r_a)$
f	frequency
F	blade force
Ma	circumferential Mach number $(=u/c_0)$
n	impeller speed
OAPWL	overall sound power level
PSD_{cx}	power spectral density of axial flow velocity fluctuation
PSD_F	power spectral density of blade force fluctuation
$\mathrm{PSD}_{\mathrm{sp}}$	power spectral density of blade surface pressure fluctuation
PSD_W	power spectral density of the acoustic power
PSDL	level of *PSD*
Re_C	Reynolds number based on chord length and w_1
$Sr_{\Lambda x}$	Strouhal number based on Λ_x and c_x
Sr^*_δ	Strouhal number based on δ^* and w_1
Tu	turbulence intensity
r_a	radius of impeller $(=D/2)$
r_i	radius of hub
t	time
u	circumferential velocity of impeller at r_a (tip velocity)
$\dot{V}$	volume flow rate
w	flow velocity in the rotating frame of reference
x, y, z	duct coordinate system (stationary frame of reference)
z	number of blades
γ	blade stagger angle
δ^*	boundary layer displacement thickness
Λ	integral length scale
ξ_1, ξ_2, ξ_3	blade coordinate system (rotating frame of reference)
ρ	fluid density
φ	flow rate coefficient

Subscripts

u	circumferential
x	axial $(=$ in the x-direction$)$

Superscripts

$'$	velocity fluctuations
$\overline{\ }$	spatial (circumferential) average

Abbreviations

BLR	boundary layer removal
IT	incident turbulence
LES	large eddy simulation
HC	honeycomb
NI	natural inflow
RPG1, RPG2	fine, coarse square-mesh array
SEM	semi-empirical noise prediction model
TBL	turbulent boundary layer
TE	trailing edge
TCS	turbulence control screen

Many semi-empirical noise prediction models (SEM) have been published for fan or wind turbine noise prediction. A simple early model is due to Sharland [1] which was fundamental for many subsequent studies on fan noise. Sharland started from a flow containing rigid surface. The surface radiates sound into the free field due to wall pressure fluctuations from incident turbulence (IT), TBL/TE interaction and TBL/blade surface interaction. Among other authors, Költzsch extended Sharland's model integrating more empirical data and taking into account a duct as proposed by Morfey [2], see Ref. [3]. The crucial assumption is always acoustic compactness, i.e. the characteristic dimensions of the surface are much smaller than the acoustic wavelength. Other semi-empirical models for a variety of airfoil self-noise mechanisms, for instance based on the experimental work on airfoil noise radiation by Brooks et al. [4], have been used by Lowson [5–7] and more recently by Moriarty and Migliore [8].

The compact source assumption is removed by non-compact linearized theories. Amiet [9] and Paterson and Amiet [10] developed analytical models for airfoil response to IT and noise which provide absolute level

prediction without recourse to empirical or adjustable constants. The noise due to turbulent flow past a TE was treated by Ffowks-Williams and Hall [11] and Amiet [12]. The blade response function for pressure fields convected past the TEs of a linear cascade of blades was investigated by Glegg [13], including a duct by Glegg and Jochault [14]. A further extension of Amiet's original formulation of TE noise is given by Roger et al. [15], accounting for all the effects of a finite chord length and aiming at the prediction from wall pressure fluctuations computed by incompressible large eddy simulation (LES).

Due to the rapid increase of computational power the numerical prediction of unsteady flow phenomena from first principles is becoming more and more feasible, yet, in complex flow fields such as in turbomachinery, it is still a demanding task. Current schemes focus more on the prediction of tonal noise due to blade/wake interaction. Algermissen et al. [16] used the unsteady Reynolds average navier–Stokes (URANS) method to predict the noise radiation of automotive cooling fans. Struts had been placed directly upstream of the fan impeller. Kouidri et al. [17] investigated the response of swept blades to a gust. Their numerical simulation yields steady and unsteady loading on the blades; the Ffowcs Williams & Hawkings formulation was used to derive the tonal part of the acoustic spectra of the unducted impeller. However, in the case of—on average—spatially uniform but temporal unsteady inflow the URANS-method fails, and the prediction of broad-band noise sources requires a high level numerical method. Thus, You et al. [18] used LES to investigate the tip clearance flow. Even more complex simulations such as the unsteady flow field in a complete mixed flow pump have been carried out by Kato et al. [19].

One goal of this study is the use of the numerical LES for broad-band fan noise prediction. For further indicative comparison a simple SEM is chosen. (As compared to the expensive LES, semi-empirical and analytical models are far more practical in an industrial environment, yet, to the knowledge of the authors, still not widely in use.) A disadvantage of any semi-empirical model based on the acoustic analogy is the unavoidable need of input: A knowledge of the statistics of the turbulent flow around or approaching the blades is required. Since the noise due to IT is very often dominant in industrial fan applications, it is a second goal of this study to provide measured turbulent inflow parameters for a variety of inflow configurations such as extremely clean inflow—achieved by a hemispherical turbulent control screen, honeycombs (HCs) and a duct boundary layer suction flow—, natural inflow (NI) and several levels of highly turbulent inflow generated by a grid type "turbulence generator".

2. Experimental setup

2.1. Investigated fan impeller

The investigated fan consists of a typical low-pressure axial impeller with six NACA 4509-blades (Fig. 1), which is running in a duct-type housing without guide vanes. The impeller outer diameter is $D = 299$ mm. For all experiments the speed is $n = 3000$ rpm (corresponding to a tip speed Mach number $Ma = u/c_0 = 0.14$, with the circumferential speed of the impeller $u = \pi Dn$ and the speed of sound c_0). The Reynolds number Re_C, based on chord length C and mean flow velocity in the rotating impeller (roughly w_1, see Fig. 3), varies from 92,000 at the hub to 170,000 at the blade tip. To indicate the fan operating point the dimensionless flow rate coefficient

$$\varphi = \frac{\dot{V}}{\left(u(\pi/4)D^2\right)}, \tag{1}$$

in preference to volume flow rate $\dot{V}$ is used. The operating point of maximum efficiency (design operating point) corresponds to $\varphi = 0.179$. This operating point or its corresponding volume flow rate was selected for most measurements within this study. Further details of the fan are listed in Table 1.

2.2. Test stand

The impeller is tested in an anechoically terminated duct test stand (following ISO 5136 [20]) with a duct diameter $D = 300$ mm (Fig. 2). The suction side of the test stand is surrounded by an anechoic chamber, not

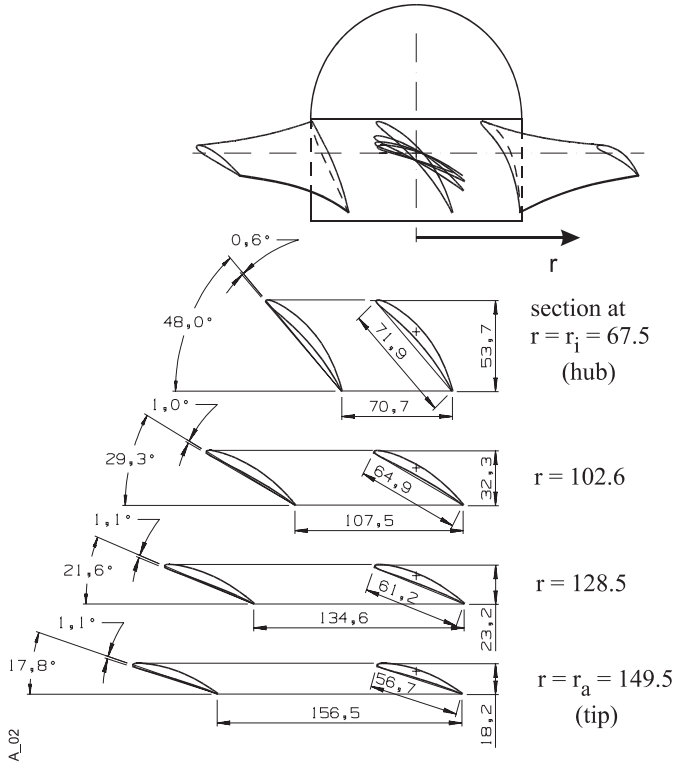

Fig. 1. Impeller investigated (if not stated otherwise, dimensions in mm).

Table 1
Fan: Data at design point and important geometrical parameters

Speed	η	3000 rpm
Volume flow rate	$\dot{V}$	0.59 m^3/s
Total to static pressure rise	Δp_{ts}	170 Pa
Total to static efficiency	η_{ts}	45%
Impeller diameter	$D = 2r_a$	0.299 m
Number of blades	z	6
Hub/tip ratio	r_i/r_a	0.45
Radial tip clearance	s/D	0.0017
Trailing edge thickness	d/D	~0.0017
	d/C	~0.0083
Fluid density (air)	ρ	1.2 kg/m^3

shown there. The volume flow rate is controlled by an adjustable throttle at the downstream side of the duct and measured by a calibrated hot film sensor.

The impeller is mounted downstream of a variety of optional devices, by which the inflow turbulence is controlled (Fig. 2 and Table 2). The NI through a bellmouth-type intake nozzle is the basic configuration; the ingested turbulence is not controlled by any further means. The porous wall duct section with an external suction flow is designed to remove the duct boundary layer (BLR) and thus to reduce wall generated turbulence. Grids are used in fluid flow studies either for the production or reduction of turbulence, and either for the creation or elimination of large-scale velocity or pressure non-uniformities. A first measure to reduce the turbulence of the NI is a layer of HC placed upstream of the impeller. Moreover, a turbulence

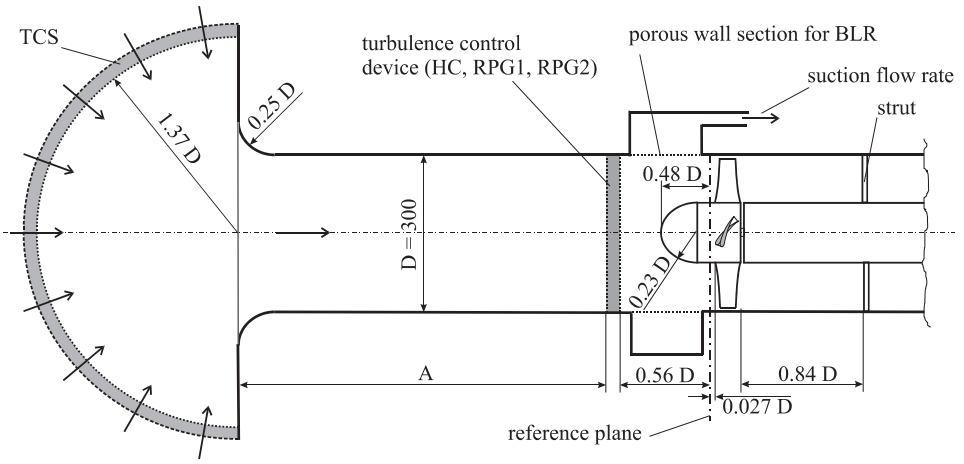

Fig. 2. Test stand (schematically); hemispherical turbulence control screen (TCS), turbulence control devices (HC, RPG1, RPG2) and duct boundary layer removal (BLR) optional; the downstream microphone with nose cone and slit tube, anechoic termination and adjustable throttle are not shown; D in mm.

hemispherical control screen (TCS) surrounding the intake nozzle, with a double layer of honeycomb and fine wire mesh according to Refs. [21,22], is used to generate an inflow with extremely low turbulence. Finally, two square-mesh arrays of square bars (RPG1 and RPG2) are designed to produce a highly turbulent inflow. Combinations of the devices allow for a large variety of inflow conditions.

The turbulence parameters are measured in a reference plane close to the leading edge plane of the impeller; the fan blades are removed but the hub is still present and non-rotating. An auxiliary fan far downstream provides the through-flow. Turbulence measurements are taken using one or two single hot-wire probes (5 μm diameter, 2 mm sensing length). They are oriented normal to the main flow direction and coupled to a standard multi-channel constant-temperature anemometry system (Dantec CTA StreamLine). The sampling rate is 20 kHz. In the case, where two probes are used, the signals are captured synchronously. The recorded data have not been corrected to account for the finite length of the hot wire.

The sound power radiated into the free field on the suction side of the fan is derived from the sound pressure measured at several positions on a control surface around the inflow [23]. The duct sound power is measured by a microphone downstream of the impeller. In order to compensate for pseudo-sound and duct mode effects, the microphone is equipped with a slit tube and a nose cone (as recommended in Ref. [11]). The overall sound power of the fan is the sum of both. Spectra are measured with a resolution of $\Delta f = 3.125$ Hz. The amplitudes of sound power spectra are presented in terms of their power spectral density (PSD) or its level PSDL. The reference pressure $p_0 = 2 \times 10^{-5}$ Pa, the reference sound power $P_0 = 10^{-12}$ W and the reference band width $\Delta f_0 = 1$ Hz.

2.3. Flow kinematics

Any local flow velocity is decomposed in a time-mean c and a fluctuating part $c'(t)$. Since all quantities are relevant in the stationary as well as in the rotating system, the different coordinate systems and flow velocity components have to be distinguished carefully (Fig. 3). The x, y, z-coordinate system is stationary and has its origin on the center line of the duct. The ξ_1, ξ_2, ξ_3-system is fixed to the rotating blade and has its origin at midchord and midspan. Given that the single hot-wire probe in the stationary system provides information on the velocity fluctuations in x-(= axial) direction c'_x, the projection $w'_2 = c'_x \cos\gamma$ is the relevant quantity, acting as the source of fluctuating loads on the blades according to the thin-airfoil linearized theory. As it is the case for any low-pressure axial fan, the blade stagger angle γ is rather small (at the outer blade sections less than 20°). Thus w'_2 is not far from c'_x and—as long as the fan operates close to its design point—w_1 not far from the circumferential speed of the impeller u.

Table 2
Investigated inflow configurations

No.	Designation	Description	Duct section length A (D) ($D = 300$ mm)
1	NI	Natural inflow through bellmouth intake	1.02
2a	BLR	Boundary layer removal	3.02
2b		by suction flow through a porous wall section	1.02
3	HC	Plane layer of 30 mm honeycomb in front of the impeller	3.02
4	RPG1	Fine square-mesh array of square bars upstream of the impeller $a \times a = 10 \times 10$ mm, $b \times b = 65 \times 65$ mm	3.02
5	RPG2	Coarse square-mesh array of square bars upstream of the impeller $a \times a = 15 \times 15$ mm, $b \times b = 60 \times 60$ mm	3.02
6	TCS	Hemispherical turbulence control screen in front of the nozzle, see Fig. 2	1.02
7	TCS + BLR	Combination of 6 and 2	1.02
8	TCS + HC	Combination of 6 and 3	1.02
9	TCS + HC + BLR	Combination of 6 and 3 and 2	1.02

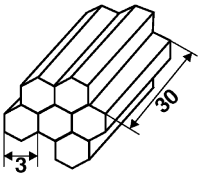

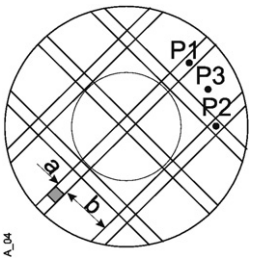

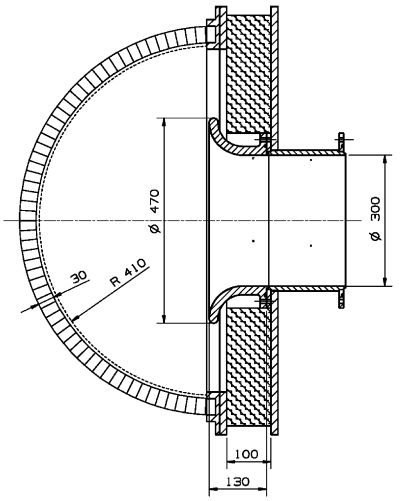

2.4. Turbulent inflow quantities

The local turbulence intensity in the blade leading edge plane

$$\mathrm{Tu} = \frac{\sqrt{\overline{c_x'^2}}}{c_x} \tag{2}$$

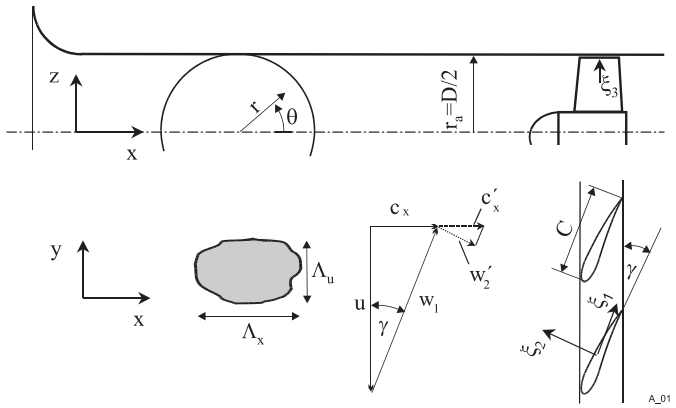

Fig. 3. Coordinate systems in the stationary and rotating frame of reference with decomposition of flow velocities (velocity triangle) and axial and circumferential correlation length of an ingested eddy.

is measured with a single hot wire probe, $\sqrt{\overline{c_x'^2}}$ being the rms value of the axial velocity fluctuations. The axial correlation length is determined assuming Taylor's "frozen turbulence"-hypothesis which allows to set $\partial/\partial t = -c_x\,\partial/\partial x$, Hinze [24]. The integral of the auto-correlation function

$$R_{xx}(\tau) = \frac{\overline{c_x'(t)c_x'(t-\tau)}}{\overline{c_x'^2}}, \tag{3}$$

yields the integral time scale

$$I = \int_0^\infty R_{xx}(\tau)\,\mathrm{d}\tau, \tag{4}$$

which is multiplied by the local axial mean velocity c_x to obtain the axial integral length scale

$$\Lambda_x = Ic_x. \tag{5}$$

Because of the small stagger angle γ of the fan blades the length scale of a turbulent eddy in spanwise direction ξ_1 (Fig. 3) of a blade corresponds more or less to the circumferential integral length scale Λ_u in the stationary system. This length scale is determined from the correlation of two hot wire signals. For any radius r, one probe is kept fixed at the 3 o'clock position (corresponding to $\theta = 0^\circ$), while the second is moved step by step counterclockwise. Thus the circumferential distance $r\theta$ is increasing from 0 mm to a maximum value, given here at 54° through practical consideration. The maximum of the correlation coefficient function $\rho_{xy}(\tau)$ is determined for each data pair (using the Matlab® Vers. 6.1 routine *xcorr*) and used to calculate the circumferential length scale

$$\Lambda_u = \int_0^\infty \max(\rho_{xy}(\tau))r\,\mathrm{d}\theta. \tag{6}$$

"Infinity" is replaced by the maximum circumferential distance [25]. Although in general the length scales are a function of the frequency, the integral length scales according to Eqs. (5) and (6) are an estimate of the largest turbulent structure encountered in the flow.

3. Semi-empirical noise prediction model (SEM)

The SEM for ducted turbomachinery used here is based on Morfey [2], Költzsch [3] and Sharland [1] and summarized as follows: A uniform hard-walled annular duct is assumed to contain a uniform steady flow on which the acoustic excitation is superimposed. Reflections at the open ends are neglected, as if the duct were infinite. Fundamental is the spectral density of the acoustic power W radiated from z uncorrelated broad-band

sources as given in [3, p. 355, Eq. (10)]:

$$\mathrm{PSD}_W(f) \equiv \frac{\mathrm{d}W(f)}{\mathrm{d}f} = \frac{\pi}{4}\frac{z}{\rho c_0^2}\frac{f}{r_a(1-(r_i/r_a)^2)^2}\,\Psi\,\mathrm{PSD}_F(f), \tag{7}$$

r_i is the hub radius, $r_a = D/2$, and ρ is the fluid density (air). The radiation factor Ψ accounts for mean flow in both the $+x$- and $-x$-direction, but it is set to 1 here because of the low axial flow Mach number. The sources are represented by the force fluctuation on a blade, PSD_F, which can be expressed in terms of the fluctuating surface pressure distribution $\mathrm{PSD}_{\mathrm{sp}}$ and their correlation area A_c

$$\mathrm{PSD}_F(f) = \iint_A \mathrm{PSD}_{\mathrm{sp}}(f,\xi_1,\xi_3)\,A_c(f,\xi_1,\xi_3)\,\mathrm{d}\xi_1\,\mathrm{d}\xi_3. \tag{8}$$

In this paper the integral in Eq. (8) is approximated by a summation over several strip-type blade elements from hub to tip (typically nine) which are assumed to radiate incoherently. A further assumption in this model is the acoustic compactness of the incoherently radiating source regions. That means that the chord length and spanwise extension of a blade strip should be clearly smaller than the wavelength of the radiated sound; this can be a rather constraining prerequisite.

For the two noise mechanisms "IT" and "TBL" the surface pressure fluctuations and the correlation area are now estimated using semi-empirical sub-models. A different empirical sub-model is used for the "TE".

3.1. IT

As depicted in Fig. 3 a turbulent eddy approaches the blade with the steady state velocity w_1 in the rotating blade coordinate system. For the time being, w_1 is assumed constant as the eddy passes the blade. Due to the turbulence the eddy has a superimposed velocity fluctuation perpendicular to the surface $w_2'(\xi_1,\xi_3,t) \ll w_1$. Following [1], the phase-delay between changes in angle of attack α' and the induced changes in lift force is neglected. (This quasi-steady approximation may provide overestimates.) Then w_2' causes a local fluctuating lift force which corresponds to a local pressure difference between the two sides of the blade

$$\Delta p'(\xi_1,\xi_3,t) = c_L'(\xi_1,\xi_3,t)\rho\frac{w_1^2}{2}, \tag{9}$$

where the lift coefficient c_L' can be written in terms of $\alpha'(t)$ due to $w_2'(t)$ by defining a lift curve slope, Φ, such that

$$c_L'(t) = c_L'(\alpha'(t)) = \Phi\,\arctan(w_2'(t)/w_1) \approx \Phi(w_2'(t)/w_1). \tag{10}$$

Hence, the mean squared pressure difference becomes

$$\overline{\Delta p'^2} = \overline{c_L'^2}\left(\rho\frac{w_1^2}{2}\right)^2 = \Phi^2\frac{\overline{w_2'^2}}{w_1^2}\left(\rho\frac{w_1^2}{2}\right)^2. \tag{11}$$

As in Ref. [1] we set $\Phi = 0.9\pi$. Defining $\mathrm{PSD}_{w2} \equiv \mathrm{d}\overline{w_2'^2}/\mathrm{d}f$ the desired power spectral density of the pressure fluctuations due to oncoming turbulence becomes

$$\mathrm{PSD}_{\mathrm{sp}} \equiv \frac{\mathrm{d}\overline{\Delta p'^2}}{\mathrm{d}f} = \frac{1}{4}(0.9\pi)^2\rho^2 w_1^2\,\mathrm{PSD}_{w2}. \tag{12}$$

For small blade angles $\gamma\,\mathrm{PSD}_{w2}$ can be approximated by the so-called one-dimensional energy spectrum $\mathrm{PSD}_{cx} \equiv \mathrm{d}\overline{c_x'^2}/\mathrm{d}f$ of the velocity fluctuation c_x'.

Numerous empirical correlations are published which give the non-dimensionalized spectrum

$$\mathrm{PSD}\,\mathrm{L}_{cx}^* \equiv 10\,\log\left(\frac{\mathrm{PSD}_{cx}}{c_x\mathrm{Tu}^2\Lambda_x}\right)\mathrm{d}B, \tag{13}$$

as a function of the Strouhal number

$$Sr_{\Lambda x} = \frac{f \Lambda_x}{c_x}. \tag{14}$$

The two correlations which have been integrated in the model described here are:

(i) A polynomial curve fit to an extensive series of measurements by Költzsch in Ref. [3]:

$$\mathrm{PSD}\, \mathrm{L}^*_{cx}(Sr_{\Lambda x}) = \sum_{k=1}^{4} a_k (\log(Sr_{\Lambda x}))^{k-1}\ \mathrm{dB} \tag{15}$$

with $a_1 = -9.784$, $a_2 = -19.001$, $a_3 = -5.548$ and $a_4 = -0.060$;

(ii) a formula from Hinze [24]

$$\mathrm{PSD}\, \mathrm{L}^*_{cx}(Sr_{\Lambda x}) = 10 \log \frac{4}{1 + (2\pi Sr_{\Lambda x})^2}\ \mathrm{dB}. \tag{16}$$

Thus, given any values for Tu and Λ_x, the power spectral density of the velocity fluctuations is known as a function of frequency. Eqs. (13) and (14) gave rise to experimentally evaluate the statistical quantities Tu and Λ_x of the turbulent inflow to the fan impeller.

The correlation area is assumed to be in the order of the size of an oncoming turbulent eddy, $A_C \propto \Lambda^2$. The frequency associated with a "frozen" turbulent eddy of length Λ moving with w is $f = w/\Lambda$, thus, $A_C \propto (w_1/f)^2$. Sharland [1] eventually proposed

$$A_C = \frac{w_1^2}{(2\pi f)^2}. \tag{17}$$

3.2. TBL

The wall pressure fluctuations, generated within the TBL, are estimated by a polynomial curve fit to measured wall pressure fluctuations on a flat blade [26] and adjusted by an empirical constant to adapt the data to rotating turbomachinery blades according to Költzsch in [3]:

$$\mathrm{PSD}_{\mathrm{sp}}(f) = \rho^2 w_1^3 \delta^* \left(\frac{0.01}{1 + 4.1985\, Sr_{\delta^*} + 0.454\, Sr_{\delta^*}^6} \right). \tag{18}$$

The relevant Strouhal-number is now defined with the boundary layer displacement thickness δ^* as

$$Sr_{\delta^*} = f \delta^* / w_1. \tag{19}$$

The displacement thickness is estimated from the well-known flat plate approximation

$$\delta^* = C 0.0518\, Re_C^{-0.2}. \tag{20}$$

The correlation area is adopted from Mugridge [27]:

$$A_C(f) = \begin{cases} \dfrac{1}{5\pi} w_1 \dfrac{1}{f} C^2 (r_a - r_i) & \text{for } \pi Sr_C \leqslant 2, \\ \dfrac{2}{5\pi^2} w_1^2 \dfrac{1}{f^2} C (r_a - r_i) & \text{for } 2 \leqslant \pi Sr_C \leqslant \dfrac{15}{\pi}, \\ \dfrac{6}{\pi^4} w_1^3 \dfrac{1}{f^3} (r_a - r_i) & \text{for } \dfrac{15}{\pi} \leqslant \pi Sr_C. \end{cases} \tag{21}$$

Here the Strouhal-number is defined with the chord length C as

$$Sr_C = fC/w_1. \tag{22}$$

3.3. TE

Out of numerous models (see Section 1) the simplest approach for the TE has been chosen. Based on the extensive measurements by Brooks et al. [4] on NACA 0012 profiles Lowson [5] developed an empirical correlation of the 1/3-octave sound pressure due to the turbulent TE flow in a distance r from the TE

$$\overline{p'^2_{\mathrm{ac,TE}}}(f) = 7.079 \times 10^{12}\, p_0^2 \delta^*\, Ma^5 (r_a - r_i) \frac{1}{r^2} G(f) \tag{23}$$

with the spectrum shape function

$$G(f) = \frac{4(f/f_{\mathrm{peak}})^{2.5}}{(1 + (f/f_{\mathrm{peak}})^{2.5})^2}, \tag{24}$$

and the peak frequency

$$f_{\mathrm{peak}} = \frac{0.02 w_1\, Ma^{-0,6}}{\delta^*}. \tag{25}$$

$p_0 = 2 \times 10^{-5}$ Pa is a reference pressure. In Eq. (23) an additional directivity function which takes account for the dipol radiation pattern has been omitted. Thus, an upper limit of the sound power is obtained by integration of the sound power as if the sound is radiated from the TE as a spherical wave

$$\mathrm{PSD}_{\mathrm{TE}}(f) = 7.079 \times 10^{12} P_0 \delta^*\, Ma^5 (r_a - r_i) \frac{4\pi}{\Delta f_{1/3\mathrm{oct}}} G(f), \tag{26}$$

where P_0 is the reference sound power 10^{-12} W and $\Delta f_{1/3\mathrm{oct}}$ is the bandwidth of each 1/3-octave band. To calculate the sound power of the complete impeller, Eq. (26) is multiplied by the number of blades z.

4. Large-eddy flow field simulation (LES)

The numerical LES method is exclusively applied to the inflow configuration RPG2 (no. 5 in Table 2). Its restricted usage for highly turbulent inflows stems from the fact that any self-noise mechanism would require an extremely fine resolution of the boundary layers in the machine which was beyond the available computer capacity. The LES-code named Frontflow Blue was developed by Kato and has been successfully applied (see e.g. Ref. [28]). It is based on a finite element discretization of the flow equations. The restriction to incompressible fluids is not relevant here because of the low value of the (circumferential) Mach number $Ma = 0.14$.

4.1. Governing equations and numerical scheme

The governing equations are the spatially filtered continuity equation and the Navier–Stokes equations in Cartesian coordinates. The velocity fluctuations are decomposed in the numerical grid scaled velocity, resolved by the LES (subscript "gs"), and the sub-grid scale velocity (subscript "sgs") which is still modeled by a turbulence model: $c'(t) = c'_{\mathrm{gs}}(t) + c'_{\mathrm{sgs}}$. In this study, the sub-grid scale velocity fluctuations are modeled with a dynamic Smagorinsky model. Since the motion of large eddies is resolved directly, a high accuracy and stability of the discretizing method is required. Conventional schemes with a high numerical dissipation are not appropriate because they will damp out the motion of eddies. Therefore a streamline upwind finite element formulation is used to discretize the governing equations. This scheme is of second-order accuracy in terms of both space and time. Details are given by Kato et al. [28,29].

4.2. Numerical grid and boundary conditions

The numerical grid is divided into four sections (Fig. 4). The first section of the grid covers the inlet section which is a cylindrical duct. At the inlet, the boundary condition is set to a uniform axial velocity. Because of the complex geometry of the square-mesh array RPG2, a static oversetting is used between the mesh array and

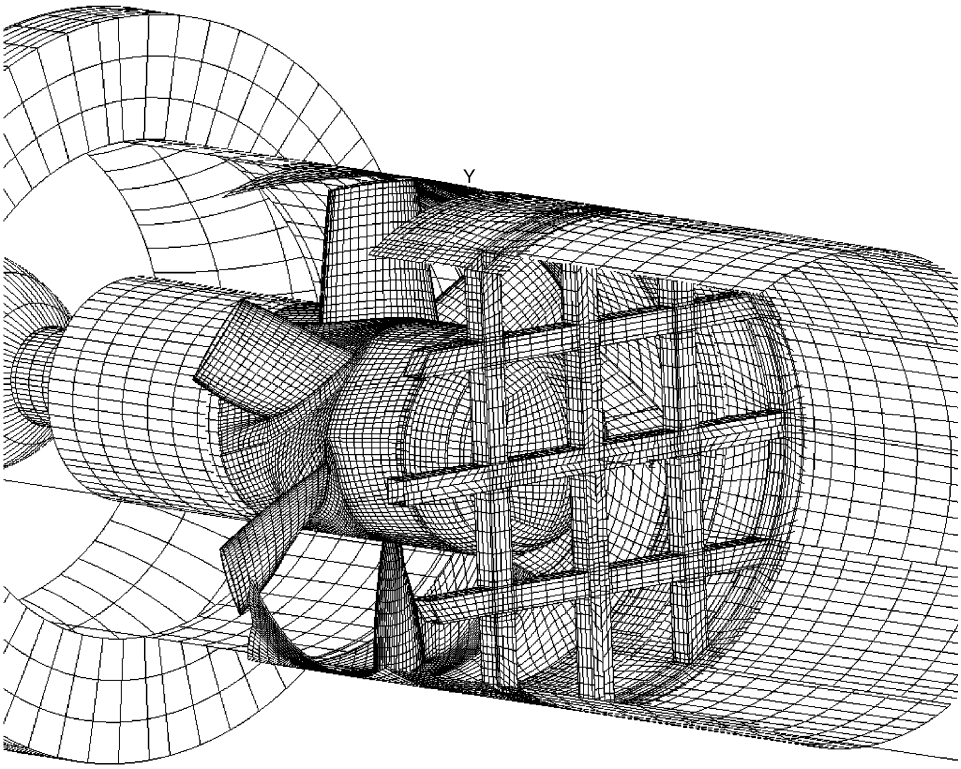

Fig. 4. Numerical grid of the complete flow domain; only every third grid point and mesh line is plotted for clarity.

the inlet section. The oversetting is dynamic between the stationary mesh array and the impeller with its rotational frame of reference. The numerical grid in a blade channel is divided into five blocks. For the near blade region, an O-topology is used. In order to reduce the computational cost the tip clearance has been neglected. The hub of the impeller is extended down to the outlet. At the outlet boundary surface the static pressure is set to zero. To avoid backflow over the outlet region during the iteration process the geometry of the outlet duct is modified such that the flow is partially accelerated. This is achieved by a diffuser-type expansion of the cross-sectional area with a subsequent contraction to the original size of the cylindrical duct-shaped housing. As compared to the impeller grid the outlet grid is coarser. This requires a third oversetting region. Non-slip wall conditions are applied to the remaining boundaries of the flow domain.

As initial conditions the velocity and the pressure is set to zero in the whole flow field. To stabilize the simulation at the beginning and to avoid pressure shock waves, an exponential start-up function is used which increases the velocity at the inlet boundary step by step. The time increment Δt_{Solv}, which is mainly determined by the stability of the simulation, is set such that 10,000 increments correspond to one single revolution of the impeller, i.e. $\Delta t_{\mathrm{Solv}} = 2 \times 10^{-6}$ s for $n = 3000$ rpm.

In order to ensure an acceptable CPU time the overall number of hexahedral elements for the whole flow domain is limited to approximately 5 millions. Still, on a Hitachi SR 8000 computer with 8 nodes and 8 CPUs each, the simulation of one impeller revolution required approximately 40 h. Further details can be found in Ref. [30].

5. Results

5.1. Statistics of the inflow turbulence

For four typical inflow configurations Fig. 5 depicts fringe plots of the measured *local* time-mean axial velocity c_x in the reference plane. c_x is non-dimensionalized with the averaged axial velocity without any

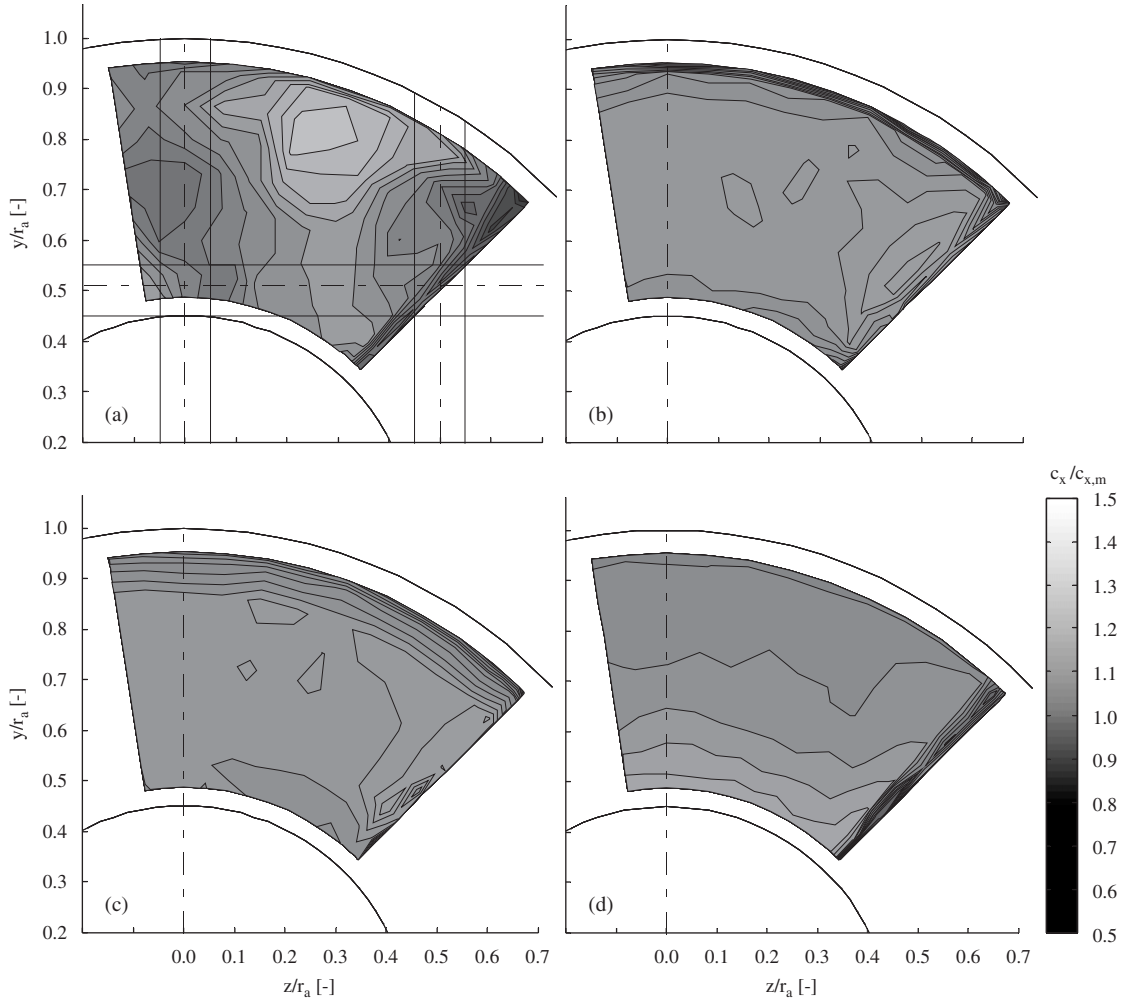

Fig. 5. Measured distribution of the local time-mean axial velocity downstream of (a) RPG2, (b) NI, (c) TCS, (d) TCS + HC + BLR.

obstructions $c_{x,m} = \dot{V}/(\pi r_a^2 - \pi r_i^2)$. RPG2 produces a distribution which is extremely non-uniform due to the wake/vortex structure downstream of the square-mesh array (Fig. 5a). The NI yields a more uniform distribution (Fig. 5b). When the turbulence control screen TCS is used the core is very uniform but the boundary layers are clearly detectable at the duct and hub wall (Fig. 5c). TCS in combination with a HC and BLR yield a uniform distribution with slightly lower velocities at the duct wall, where the suction is applied (Fig. 5d). Each plot shows distortions of the maps at the right-hand side boundary at the 2 o'clock position, corresponding to $\theta = 0^\circ$. These are caused by the wake of the second fixed hot-wire probe, placed slightly upstream at $\theta = 0^\circ$ as well. Therefore, for the following quantitative analysis of the data the region from $\theta = 0$–5° for all radii is excluded. Fig. 6 throws further light on details of the flow field in the reference plane. It presents—as a function of the radius—*circumferentially averaged* (indicated by the bar above the symbol) time-mean velocities, turbulence intensities and length scales. Clearly, the velocity is almost independent of all turbulence control devices and not significantly influenced by the radial position. However, turbulence intensity and integral length scales vary considerably. (Note, that the boundary layer could not be fully detected because of the absolute size of the hot wire probe.) RPG2 produces turbulence intensities as high as 21% (Fig. 6a). TCS reduces $\overline{\mathrm{Tu}}$ down to less than 1% in the core region but not in the vicinity of the duct wall (Fig. 6c). The combination of TCS, HC and BLR yields an extremely uniform $\overline{\mathrm{Tu}}$-distribution (Fig. 6d). At the same time this combination produces the smallest integral length scales. Clearly, the length scales are the

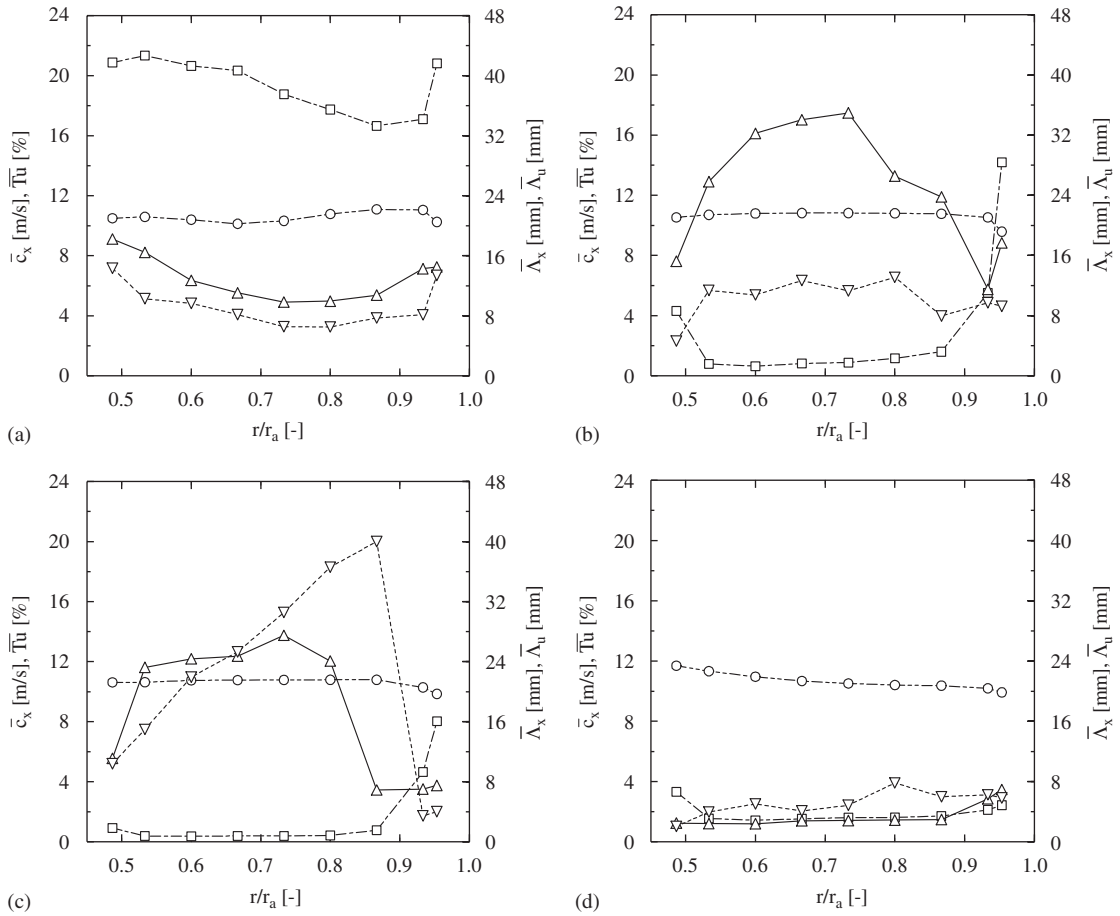

Fig. 6. Measured turbulent inflow parameters as a function of the radius in the reference plane; (a) RPG2, (b) NI, (c) TCS, (d) TCS + HC + BLR; ○: $\overline{c_x}$, □: $\overline{\mathrm{Tu}}$, △: $\overline{\Lambda_x}$, ▽: $\overline{\Lambda_u}$; the bars indicate a spatial averaging of the quantity in circumferential direction.

largest with NI as well as with TCS. As shown in Section 5.2 and as expected, the combination of TCS, HC and BLR produces the lowest fan noise. Data for all turbulence control devices investigated within this project are published in Ref. [31]. Table 3 lists numerical values of the circumferentially averaged turbulent parameters and the ratio $\overline{\Lambda_x}/\overline{\Lambda_u}$ from tip to hub. In general, $\overline{\Lambda_x}$ and $\overline{\Lambda_u}$ have the same order of magnitude, but in many cases $\overline{\Lambda_x}$ tends to be slightly larger than $\overline{\Lambda_u}$. According to Roach [32] several previous workers have found $\Lambda_x \approx 1.9\Lambda_u$. In case of mesh generated turbulence, Roach also presented an empirical correlation $\Lambda_x/a = 0.2\sqrt{\Delta x/a}$, where Δx is the distance downstream from the turbulence control device and a is the bar width of the mesh array. Measurements made agree reasonably well with Roach's results.

Three one-dimensional energy spectra for the inflow configurations TCS, BLR and RPG2, non-dimensionalized as defined in Eq. (13), are presented in Fig. 7. They were measured with a single hot wire at a monitoring point not too far away from the duct wall. The spectra coalesce and are correctly predicted by either Eq. (15) or (16). Although not shown, the data for all other inflow configurations and monitoring points fit well.

A comparison of the LES-predicted and measured distribution of the time-mean axial velocity in the reference plane is shown in Fig. 8. The wake/vortex structure due to the coarse square-mesh array RPG2 agrees quantitatively and qualitatively well with the experimental data. Further LES-predicted results are presented at three different monitoring points in the reference plane (Fig. 9). The three monitoring points are selected as indicated in Table 2: P1 just behind a bar of RPG2, P2 behind a joint of two bars, and P3 behind an open area between two bars. At these points the local turbulence intensity, the axial integral length scale and

Table 3
Measured turbulence statistics

Inflow configuration				Range of the measured turbulent parameters from hub to tip (spatially averaged in circumferential direction; flow rate corresponding to $\varphi = 0.179$)			
No.	Designation	Description	Duct section length A (D)	$\overline{\Lambda_x}$ (mm)	$\overline{\Lambda_u}$ (mm)	$\overline{\Lambda_x}/\overline{\Lambda_u}$ (−)	$\overline{\mathrm{Tu}}$ (%)
1	NI	Natural inflow through bellmouth	1.02	12–35	5–13	1.2–3.3	0.6–14.2
2a	BLR	Boundary layer removal	3.02	9–28	5–13	1.2–2.6	0.6–9.4
2b			1.02	7–28	4–18	1.1–3.4	1.0–11.6
3	HC	Plane layer of honeycomb	3.02	3–15	4–12	0.7–1.8	1.4–13.5
4	RPG1	Fine square-mesh array $a \times a = 10 \times 10$ mm, $b \times b = 65 \times 65$ mm	3.02	9–16	5–16	0.9–2.2	12.5–20.9
5	RPG2	Coarse square-mesh array $a \times a = 15 \times 15$ mm, $b \times b = 60 \times 60$ mm	3.02	10–18	7–14	1.1–1.8	16.7–21.3
6	TCS	Hemispherical turbulence control screen	1.02	7–28	3–40	0.2–2.0	0.4–8.0
7	TCS + BLR	Combination of 6 and 2b	1.02	1–8	3–24	0.1–3.3	0.5–5.0
8	TCS + HC	Combination of 6 and 3	1.02	2–7	2–14	0.3–2.1	1.3–13.4
9	TCS + HC + BLR	Combination of 6 and 3 and 2b	1.02	2–7	2–8	0.4–1.2	1.4–3.3

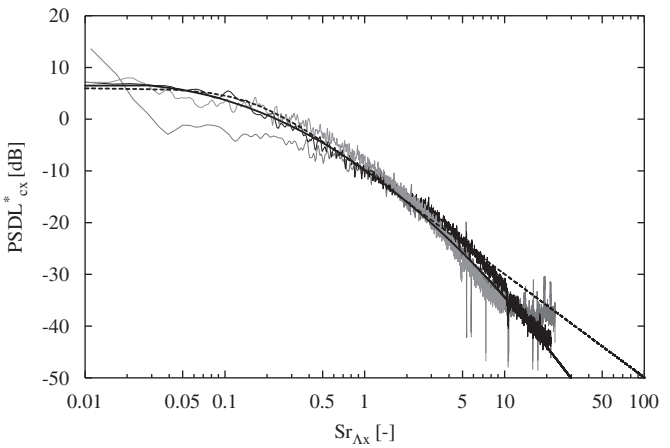

Fig. 7. Collapse of the non-dimensionalised energy spectra of the axial velocity fluctuations in the reference plane at $r/r_a = 0.96$, $\theta = 0°$; measurement with TCS, BLR and RPG2 (————), correlation from Hinze Eq. (15) (- - - - - - - - -), correlation from Költzsch Eq. (16) (————).

the time-mean axial velocity are calculated. Given the uncertainties in the measurements, the agreement between prediction and measurement is very satisfactory.

The power spectral density of the axial velocity fluctuations at monitoring point P2 is depicted in Fig. 10. As compared to the experimental data the LES results agree well up to the "cut-off frequency" due to the filtering of the LES-method, corresponding to a Strouhal number of 0.4 (≈ 300 Hz).

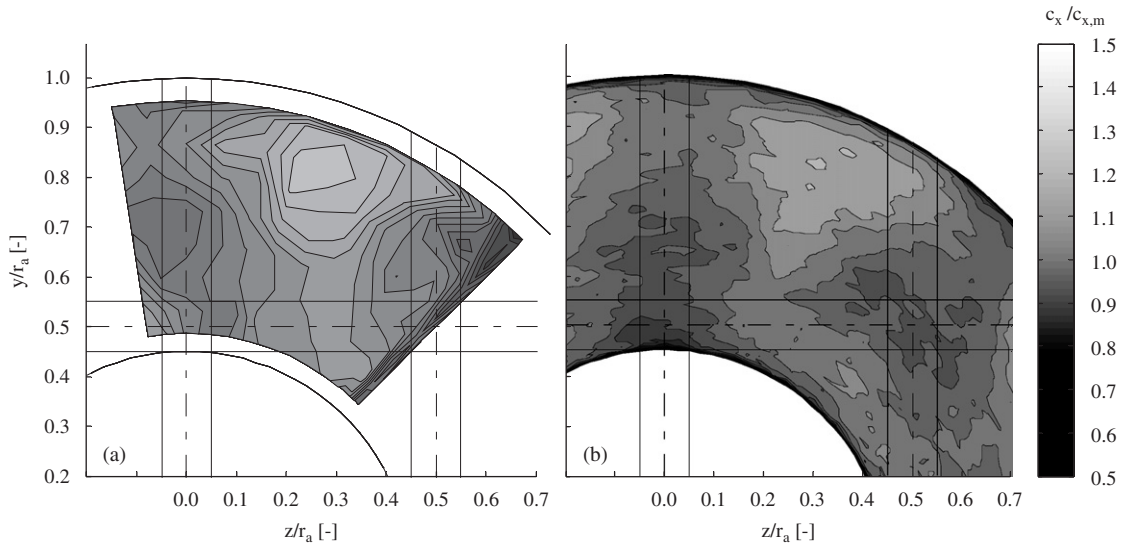

Fig. 8. Local mean velocity distribution downstream of RPG2 in the reference plane; (a) measurement, (b) LES-prediction.

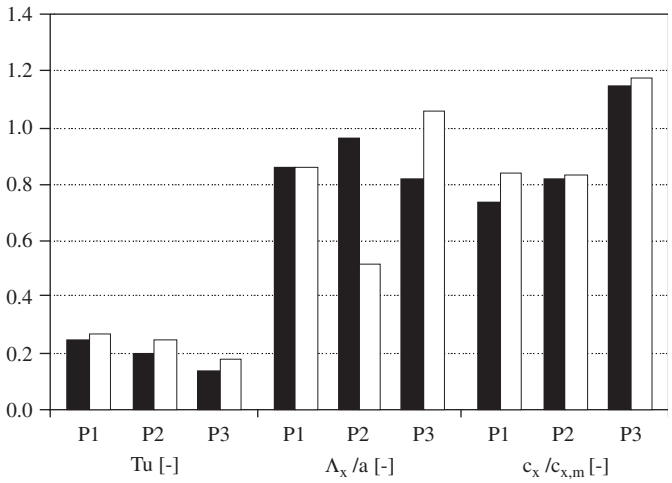

Fig. 9. Local turbulence intensity, integral length scale and time-mean flow velocity downstream of RPG2 in the reference plane at three monitoring points P1, P2 and P3 (see Table 2): LES-prediction (white bars) vs. measurements (black bars).

5.2. SEM-predicted and measured fan noise

A merit of the SEM is that the spectral contribution from each source to the overall spectrum can be quantified (Fig. 11). The TE contributes the least, the TBL is the dominant source in the high-frequency range and for turbulent inflow—depending on its turbulence intensity—in the low-frequency range. The influence of Tu is considerable (Fig. 12). Even for moderate turbulence intensities, the turbulent inflow mechanism becomes dominant in the low-frequency range.

Figs. 13 and 16 show measured and SEM-predicted sound power spectra. Strictly speaking—because of the assumption of acoustically compact sources—the comparison of predicted and measured broad-band noise is valid only in the frequency region up to 1 kHz, where the chord length is clearly smaller than the wavelength of the radiated sound. Given all other assumptions (duct without reflecting boundaries (Eq. (7)), quasi-steady lift force response to ingested turbulence (Eq. (10)), Költzsch's empirical constant in the wall pressure fluctuations beneath a TBL (Eq. (18)) and the sound power from a simplified TE sound field (Eq. (26))), the SEM predicts

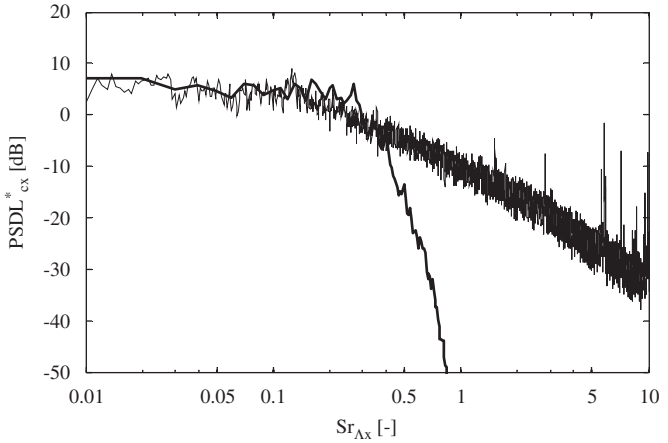

Fig. 10. Non-dimensionalized power spectral density of the axial velocity fluctuations in the reference plane at monitoring point P3; measured (————), LES-predicted (———).

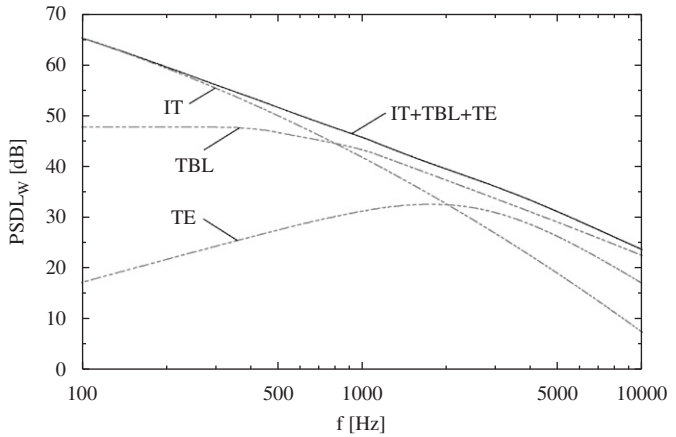

Fig. 11. Contributions to the overall spectrum from the three noise mechanisms TE (= trailing edge), TBL (= turbulent boundary layer) and IT (= incident turbulence) as predicted with SEM; data correspond to inflow configuration NI; ref 10^{-12} W/Hz.

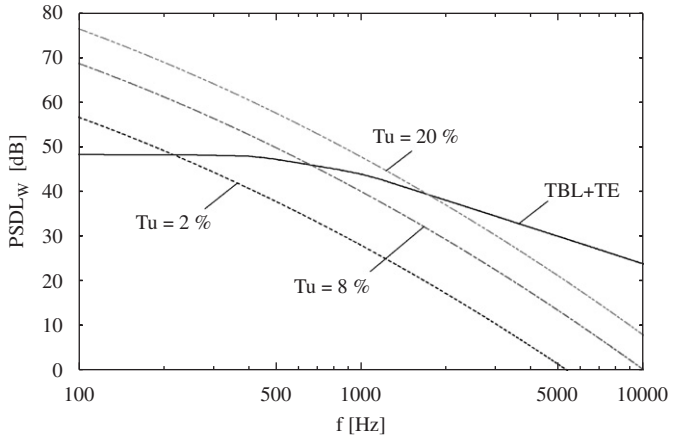

Fig. 12. Influence of turbulence intensity on the overall spectrum as predicted with SEM; Λ is set to a constant value of 35 mm; ref 10^{-12} W/Hz.

the spectra reasonably well without otherwise tuning any parameters. It is worth mentioning that BLR reduces the broad-band levels between 1 and 5 kHz. As seen in Fig. 16, RPG2 increases the low frequency broad-band levels up to 1 kHz.

Surprisingly all measured spectra show peaks at multiples of BPF which of course are not predicted by the SEM. In order to eliminate sources of these tonal components in the experiments a number of measures have been investigated such as an increased precision of the geometry of the inflow nozzle and the tip clearance, a minimization of the wobble and the unbalance of the impeller and a variation of the impeller speed. However, none of these measures were successful in eliminating the tonal components completely. They seem to be attributed to a large-scale stationary circumferential inflow disturbance due to a slightly asymmetric inflow from the laboratory environment.

Fig. 14 shows the measured and the SEM-predicted overall sound power levels of the fan for a number of operating points φ (see Eq. (1)). Peaks at multiples of blade passing and impeller shaft frequency had been removed in the underlying measured frequency spectra. One should not focus on operating points smaller than $\varphi = 0.17$, because stall—which is not modeled here—more and more dominates the noise. Again, it is remarkable, how much the noise in the "healthy" region of fan operation is determined by the inflow turbulence. The combination TCS + HC + BLR yields the lowest noise levels which is believed to be more or less the pure self-noise of the fan. The SEM predicts the measured tendencies correctly. The higher the turbulence level, the better is the quantitative agreement. Obviously—and as expected—the more accurate prediction of the self-noise requires refined models.

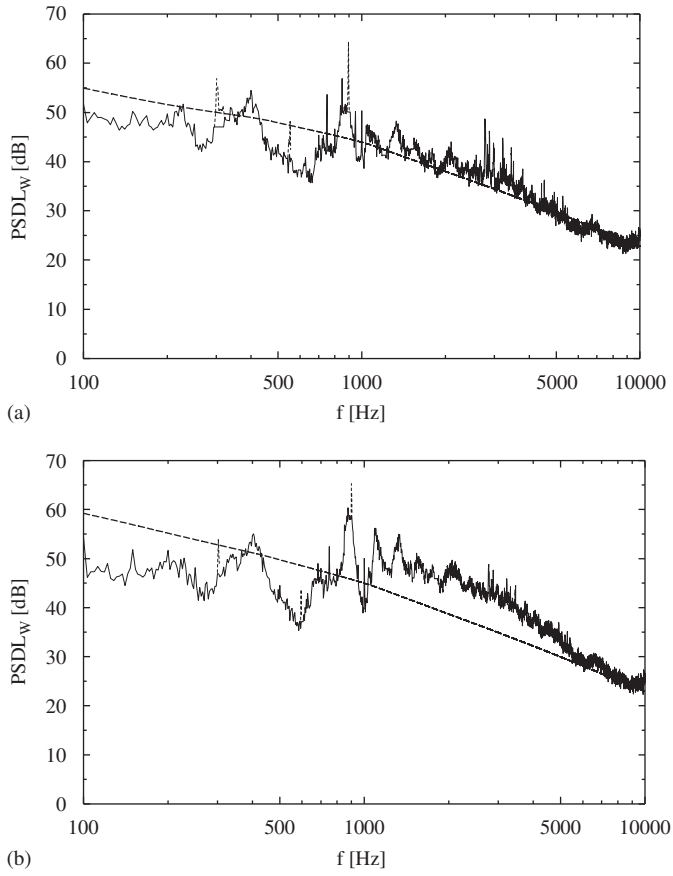

Fig. 13. Measured (————) and SEM (- - - - - - - - -) predicted sound power spectra; (a) TCS + BLR, (b) TCS; ref 10^{-12} W/Hz; tones at multiples of BPF in the measured data are dashed.

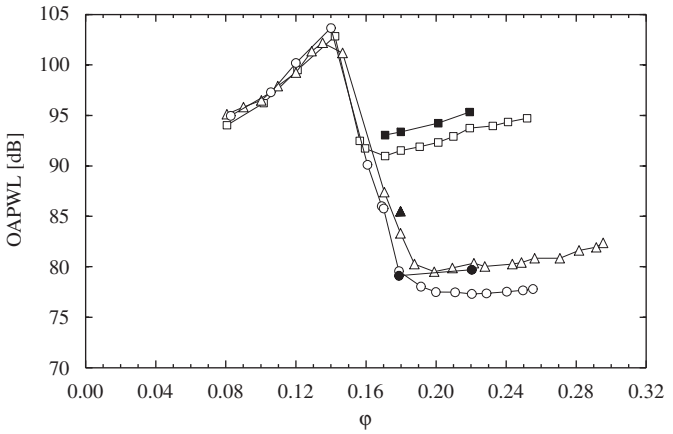

Fig. 14. Measured (peaks at multiples of impeller shaft frequency removed) and SEM-predicted overall sound power levels (ref 10^{-12} W) as a function of the fan's flow rate coefficient φ; □: RPG2, △: NI, ○: TCS + HC + BLR, filled plot symbols indicate the corresponding SEM-prediction.

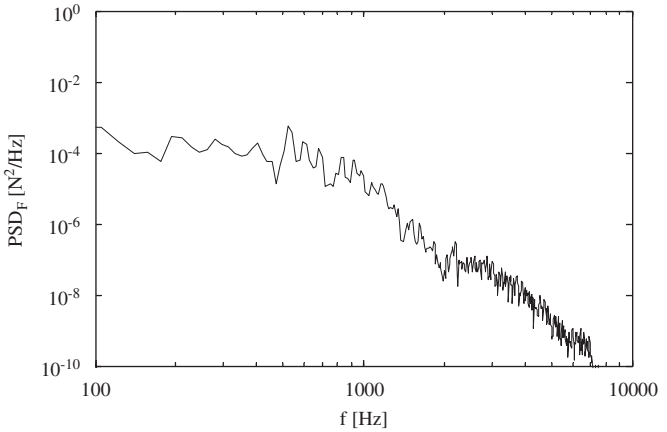

Fig. 15. LES-predicted unsteady impeller force (RPG2).

5.3. LES-predicted fan noise spectrum

As already mentioned the LES is exclusively applied to the inflow configuration RPG2. The discussion and post-processing of the unsteady flow field data are based on a time interval of LES-predicted data which does not include the physically non-relevant period during start up from the initial condition. In general, the time interval considered corresponds to 10 revolutions of the impeller. The power spectral density is estimated by dividing the discrete-time signal into seven 50%-overlapping sections, then applying a Hanning window and averaging the spectra from all sections.

The unsteady overall impeller force is evaluated by a numerical integration of the unsteady pressures over each blade surface element of the impeller. Fig. 15 depicts the power spectral density of the thus obtained force PSD_F.

Using Eq. (7) and substituting $z\,PSD_F$ by the overall impeller force gives the sound power spectrum as shown in Fig. 16. The "erroneous" tonal components in the experimental data are dashed. In general, the agreement between the LES predicted and the measured sound spectrum is reasonably good. Reasons for the deviation at some frequencies are the inaccurate resolution of the blade boundary layer, the neglected tip clearance, and, after all, the limitations of the acoustical model with respect to acoustic compactness.

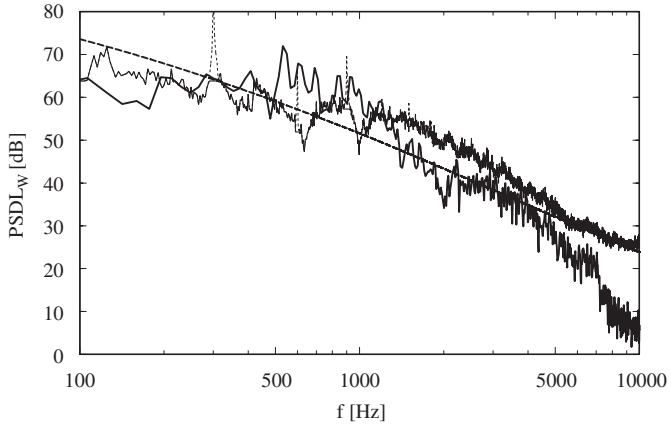

Fig. 16. Fan sound power spectra (RPG2); measured (————), SEM (- - - - - - - - - -) and LES (————) predicted; tones at multiples of BPF in the measured data are dashed; ref 10^{-12} W/Hz.

With regard to the limits of the frequency resolution, the LES is able to resolve velocity fluctuations downstream of the turbulence generator up to approx. 300 Hz with the numerical grid as described. However, the radiated sound is predicted reasonably correctly far above 1000 Hz. This is due to the fact that the convection velocity of the turbulent eddies over the involved solid surfaces varies roughly by a factor of 5. In the turbulence generating mesh array, the convection velocity is in the order of the axial velocity in the stationary frame of reference, whereas over the blade surfaces the eddies are convected with approximately the relative velocity in the rotating frame of reference. The kinematics in low-pressure fans is typically such that the axial velocity is much smaller than the circumferential and thus the relative velocity. Hence, assuming a size of turbulent eddies which does not vary as the eddies are convected, the increase of convection velocity by a factor 5 leads to a captured frequency range up to 1500 Hz in the force fluctuations on the blades and subsequently in the acoustic spectra.

6. Conclusions

A special merit of the SEM is the fact that the spectral contribution to the overall spectrum from each source is quantified separately. In order to predict the—in many industrial fan applications dominant—"turbulent ingestion noise", the intensity and the integral length scale of the ingested turbulence must be given. This requires a "catalog" from which one can take these data for realistic inflow configurations. In this study the turbulent inflow parameters have been determined experimentally for a variety of inflow configurations. A hemispherical turbulent control screen surrounding the bellmouth-type inlet and other measures have reduced the turbulence intensity of the inflow to the impeller to less than 1%. On the other hand a grid-type "turbulence generator" provided more than 20% turbulence intensity. As already demonstrated in previous studies from other authors the SEM is very easy to apply and requires very little computational effort. Here, it predicts reasonably well the influence of the fan operating point and the nature of the inflow on the noise spectra—without any further tuning of parameters. However, the predicted noise spectra appear unrealistically "smooth", since the underlying empirical data is averaged and modeled in the frequency domain. The SEM is not able to capture details of the fan geometry such as the form of the blade profile or shape (e.g. skewed) or flow phenomena such as flow separation. A systematic drawback of the here employed SEM is that it does not reproduce the cut-off of the broad-band noise spectrum; this inability to predict properly sound from non-compact sources would have been palliated by finer analytical non-compact models. Nevertheless, the SEM-predicted *overall* sound power levels are in good agreement with measurements—thanks to averaging due to integration.

The LES allows to compute the acoustic sources, i.e. the fluctuating force on the blades, in the time domain from first principles. Since the source prediction is based on the flow through the true geometry of the impeller

and the machine, the method yields inherently the influence of geometric details. So far the effect of the ingested turbulence on the sound sources and the fan noise has been predicted surprisingly well. Details of the source characteristics and their origin, averaged out in SEM, are obtained. Numerical experiments to predict the pure self-noise, however, failed and are not reported here; in order to capture these effects a finer resolution of the wall boundary layer is essential. This would require an increase of the size of the numerical grid which easily can be beyond the scope of available computer capacity. Even for the reported case of highly turbulent inflow, the computational cost are immense. Further improvements are expected by taking into account additional geometric features such as the tip clearance which was omitted because of computational resources. The acoustic results presented are based on a rather restricted acoustic model. Strictly speaking the model is valid only for incoherent blade forces, i.e. without interaction or phase shift between the single blades. Therefore, refined modeling of the sound field should also improve the accuracy of the predicted noise.

Acknowledgements

Parts of the work were supported by the ''Bundesministerium für Wirtschaft über die Arbeitsgemeinschaft industrieller Forschungsvereinigungen'' Otto von Guericke ''e.V. (AiF)'' of the Federal Republic of Germany and the German Research Foundation (DFG). The authors express their appreciation to C. Kato of the University of Tokyo. Supported by the German Academic Exchange Service (DAAD) Prof. Kato hosted the third author for more than a year in his research group. We gratefully acknowledge all this support.

References

[1] I.J. Sharland, Sources of noise in axial flow fans, *Journal of Sound and Vibration* 1 (3) (1964) 302–322.
[2] C.L. Morfey, The acoustic of axial flow machines, *Journal of Sound and Vibration* 22 (4) (1972) 445–466.
[3] L. Bommes, J. Fricke, R. Grundmann (Eds.), *Ventilatoren. 2*. Auflage, Vulkan Verlag, Essen, 2003 pp. 352–377.
[4] F.T. Brooks, D.S. Pope, M.A. Marcolini, Airfoil self-noise and prediction, NASA RP-1218, 1989.
[5] M.V. Lowson, Assessment and prediction of wind turbine noise, Flow Solutions Report 92/19, ETSU W/13/00284/REP, December 1992, pp. 1–59
[6] M.V. Lowson, S.P. Fiddes, Design prediction model for wind turbine noise: 1. Basic aerodynamic and acoustic models, Flow Solution Report 93/06, W/13/00317/00/00, November 1993, pp. 1–46.
[7] M.V. Lowson, Theory and experiment for wind turbine noise, AIAA Paper 94-0119, 1994.
[8] P. Moriarty, P. Migliore, Semi-empirical aeroacoustic noise prediction code for wind turbines, Technical Report National Renewable Energy Laboratory/TP-500-34478, 2003.
[9] R.K. Amiet, Acoustic radiation from an airfoil in a turbulent stream, *Journal of Sound and Vibration* 41 (4) (1975) 407–420.
[10] R.W. Paterson, R.K. Amiet, Noise and surface pressure response of an airfoil to incident turbulence, *Journal of Aircraft* 14 (8) (1977).
[11] J.E. Ffowks-Williams, L.H. Hall, Aerodynamic sound generation by turbulent flow in the vicinity of a scattered half plane, *Journal of Fluid Mechanics* 40 (4) (1970) 657–670.
[12] R.K. Amiet, Noise due to turbulent flow past a trailing edge, *Journal of Sound and Vibration* 47 (3) (1976) 387–393.
[13] S.A.L. Glegg, Airfoil self noise generated in a cascade, AIAA Paper No. 96-1739, 1996.
[14] S.A.L. Glegg, C. Jochault, Broadband self noise from a ducted fan, AIAA Paper 97-1612, 1997.
[15] M. Roger, S. Moreau, M. Wang, An analytical model for predicting airfoil self-noise using wall-pressure statistics, Annual Research Briefs, Center for Turbulence Research, Ecole Centrale de Lyon, 2002, pp. 405–414.
[16] G. Algermissen, R. Siegert, Th. Spindler, Numerical simulation of aeroacoustic sound generated by fans under installation conditions, AIAA Paper No. 2001-2174, 2001.
[17] S. Kouidri, D. Fedala, T. Belamri, R. Rey, Comparative study of the aeroacoustic behaviour of two axial flow fans with different sweep angles, *ASME Fluid Engineering Summer Conference*, Paper No. FEDSM2005-77424, Houston, TX, 2005.
[18] D. You, M. Wang, R. Mittal, P. Moin, Study of rotor tip-clearance flow using large-eddy simulation, *AIAA Journal* No. 2003-0838, (2003).
[19] C. Kato, H. Mukai, A. Manabe, Large eddy simulation of unsteady flow in a mixed-flow pump, *The Ninth International Symposium on Transport Phenomena and Dynamics of Rotating Machinery*, Honolulu, Hawaii, 2002.
[20] ISO 5136, Determination of sound power radiated into a duct by fans, 1990.
[21] J. Scoles, J.B. Ollerhead, An experimental study of the effects of an inlet flow conditioner on the noise of a low speed axial flow fan, National Gas Turbine Establishment, Report No. AT/2170/049/XR, University of Technology, Loughborough, 1981.
[22] J. Scheimann, J.D. Brooks, Comparison of experimental and theoretical turbulence reduction from screens, honeycomb and honeycomb–screen-combinations, *Journal of Aircraft* 18 (8) (1981).
[23] ISO 3745, Determination of sound power levels of noise sources using sound pressure—precision methods for anechoic and hemi-anechoic rooms, 2000.

[24] J.O. Hinze, *Turbulence*, 2nd ed., McGraw-Hill, 1975.
[25] A.V. Smol'yakov, V.M. Tkachenko, *The Measurement of Turbulent Fluctuations*, Springer, Berlin, Heidelberg, New York, 1983.
[26] W.L. Keith, D.A. Hurdis, B.M. Abraham, A comparison of the turbulent wall-pressure spectra, *Transactions of the ASME, Journal of Fluids Engineering* 114 (1992) 338–347.
[27] B.D. Mugridge, Broadband noise generation by aerofoils and axial flow fans, AIAA Paper 73-1018, 1973.
[28] C. Kato, M. Kaiho, A. Manabe, An overset finite element large eddy simulation method with application to turbomachinery and aeroacoustics, *Journal Applied Mechanics* (70) (2003) 32–43.
[29] C. Kato, M. Ikegawa, Large eddy simulation of unsteady turbulent wake of a circular cylinder using the finite element method, *Advances in Numerical Simulation of Turbulent Flows, ASME FED* 117 (1991) 49–56.
[30] H. Reese, C. Kato, Th., Carolus, Large eddy simulation of acoustical sources in a low pressure axial-flow fan due to highly turbulent inflow conditions, Seisan Kenkyu, 57(1), January 2005, Tokyo, Japan.
[31] M. Schneider, Der Einfluss der Zustrombedingungen auf das breitbandige Geräusch eines Axialventilators (Dr.-Ing. Dissertation Universität Siegen, 2005), Fortschritt-Berichte VDI Reihe 7 Nr. 478. Düsseldorf: VDI Verlag 2006.
[32] P.E. Roach, The generation of nearly isotropic turbulence by means of grids, *International Journal Heat and Fluid Flow* 8 (2) (1986) 82–92.